Han et al. *EPJ Quantum Technology* (2023) 10:28
https://doi.org/10.1140/epjqt/s40507-023-00184-z

EPJ Quantum Technology
a SpringerOpen Journal

RESEARCH

Open Access

Microwave electrometry with bichromatic electromagnetically induced transparency in Rydberg atoms

Mingzhi Han[1], He Hao[2*], Xiaoyun Song[1], Zheng Yin[1], Michal Parniak[3], Zhengmao Jia[1] and Yandong Peng[1*]

*Correspondence:
Hehao@casic.com.cn;
pengyd@sdust.edu.cn
[1]Qingdao Key Laboratory of Terahertz Technology, College of Electronic and Information Engineering, Shandong University of Science and Technology, Qingdao 266590, China
[2]Beijing Institute of Radio Measurement, Beijing, China
Full list of author information is available at the end of the article

Abstract

A scheme for measuring microwave (MW) electric (E) fields is proposed based on bichromatic electromagnetically induced transparency (EIT) in Rydberg atoms. A bichromatic control field drives the excited state transition, whose absorption shows three EIT windows. When a MW field drives the Rydberg transition, the EIT windows split and six transmission peaks appear. It is interesting to find that the peak-to-peak distance of transmission spectrum is sensitive to the MW field strength, which can be used to measure MW E-field. Simulation results show that the spectral resolution could be increased by about 4 times, and the minimum detectable strength of the MW E-field may be improved by about 3 times compared with the common EIT scheme. After the Doppler averaging, the minimum detectable MW E-field strength is about 5 times larger than that without Doppler effect. Also, we investigate other effects on the sensitivity of the system.

Keywords: Bichromatic electromagnetically induced transparency; Microwave electric field measurement; Rydberg atoms; Doppler effect

1 Introduction

Microwave (MW) electric (E) field measurement has great technological importance in electronic information systems, which have been widely used in radar [1, 2], communications [3–5], navigation [6, 7], remote sensing [8], etc. Traditional MW measurement is based on dipole antennas, which is limited to receiving sensitivity, self-calibration, antenna size and so on [9]. Rydberg atoms have large electric dipole moments, which are extremely sensitive to external electric field [10]. Rydberg atom-based MW metrology has been explored with quantum technology [11–13], e.g., electromagnetically induced transparency (EIT) [14–17], Autler-Townes (AT) splitting [18, 19], electromagnetically induced absorption (EIA) [20, 21], and active Raman gain (ARG) [22, 23]. At present, many promising schemes have been proposed for measuring MW fields, using frequency detuning [24], homodyne detection [25], intracavity atomic systems [26], double dark states [27, 28], dispersion [29], nonlinear effects [30] and deep learning [31], etc.

Bichromatic EIT can improve the fluorescence, absorption and transmission spectra of atoms [32–34]. Wang et al. first experimentally demonstrated bichromatic EIT in cold atoms and observed multiple absorption peaks [35]. Later, Yan et al. experimentally observed double symmetrical EIT windows instead of multiple absorption peaks in hot atomic vapors [36]. In recent years, four-wave mixing (FWM) signals in such systems has attracted great interest [37–39]. For example, multi-channel FWM process [40], phase compensation induced by anomalous dispersion [41], and high-efficiency reflection [42]. Also, bichromatic field has other important applications, such as optical nonreciprocity [43], optical bistability [44], optomechanical bichromatic wavelength switching [45], multimode circuit electromechanical systems [46], cross-phase modulation [47], and attosecond polarization [48]. While, few research involves the application of bichromatic EIT in MW E-field measurement.

Here, we present a scheme for MW E-field measurement by using bichromatic EIT in Rydberg atoms. First, a Doppler-free configuration is considered, where the probe field counter-propagates with the bichromatic control field. When the bichromatic control field drives the excited state transition, the EIT spectrum shows three transmission peaks. With coupling of a MW field, the transmission peaks split into six. The frequency splitting of the transmission peaks is linearly related to the MW field strength. This can be used to measure MW E-field. The numerical results show that the linewidth of the central transmission peaks may be narrowed to 1/4 of the common EIT scheme, and the minimum detectable strength of the MW E-field could be improved by about 3 times. Fortunately, if the probe and bichromatic control fields co-propagate through the atomic vapor, the Doppler effect greatly narrows the central transmission peaks, and the minimum detectable MW E-field strength is about 5 times larger than that without Doppler effect. The scheme may be useful for designing novel MW sensing devices.

2 Model and basic equations

The four-level Rydberg atomic system we considered is shown in Fig. 1(a). A bichromatic control field $E_c(t) = (E_{c1}e^{-i\omega_{c1}t} + E_{c2}e^{-i\omega_{c2}t})/2 + c.c.$ drives the transition $|2\rangle \rightarrow |3\rangle$ with frequency difference $\omega_{c2} - \omega_{c1} = \delta$. A weak probe field $E_p(t) = E_p e^{-i\omega_p t}/2 + c.c.$ drives the transition $|1\rangle \rightarrow |2\rangle$, and a MW field $E_m(t) = E_m e^{-i\omega_m t}/2 + c.c.$ drives the Rydberg transition $|3\rangle \rightarrow |4\rangle$. The relevant quantum states $|1\rangle$, $|2\rangle$, $|3\rangle$ and $|4\rangle$ correspond to the rubidium-87 atomic levels $5S_{1/2}(F = 2)$, $5P_{3/2}(F = 3)$, $53D_{5/2}$, and $54P_{5/2}$, respectively. Figure 1(c) shows the schematic configuration of the coupling fields and the atomic vapor cell. The probe and bichromatic control fields counter-propagate through the atomic vapour, which belongs to a Doppler-free scheme.

After the electric dipole approximation, the Hamiltonian of the system in the interaction picture is given by [49]

$$\begin{aligned} H = {} & \hbar\omega_1|1\rangle\langle 1| + \hbar\omega_2|2\rangle\langle 2| + \hbar\omega_3|3\rangle\langle 3| + \hbar\omega_4|4\rangle\langle 4| \\ & - \hbar\big[\Omega_p e^{-i\omega_p t}|2\rangle\langle 1| + \big(\Omega_{c1}e^{-i\omega_{c1}t} + \Omega_{c2}e^{-i\omega_{c2}t}\big)|3\rangle\langle 2| \\ & + \Omega_m e^{-i\omega_m t}|4\rangle\langle 3| + H.C.\big], \end{aligned} \tag{1}$$

where the Rabi frequencies of the probe, control, and MW fields are, respectively, denoted as $\Omega_p = E_p\mu_{12}/\hbar$, $\Omega_{c1(c2)} = E_{c1(c2)}\mu_{23}/\hbar$ and $\Omega_m = E_m\mu_{34}/\hbar$. μ_{ij} and ω_{ij} are the relevant dipole

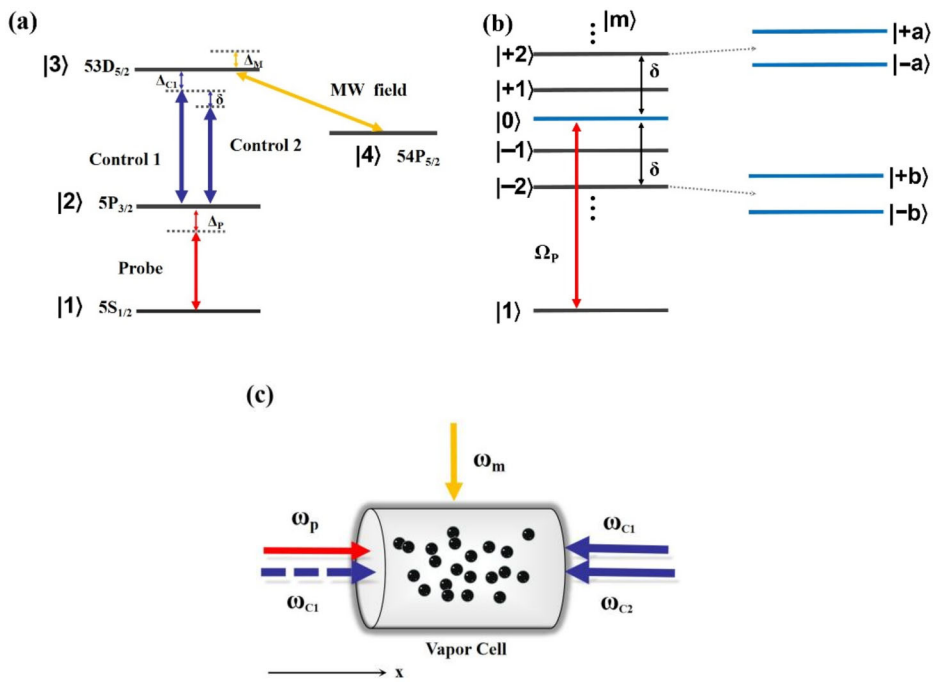

Figure 1 (a) Four-level Rydberg atomic model, (b) the corresponding dressed picture and (c) schematic diagram of the experiment

moment and transition frequency from $|i\rangle$ to $|j\rangle$ $(i,j \in \{1,2,3,4\})$. E_p, $E_{c1(c2)}$, and E_m are the respective amplitudes of the laser fields. The dynamic evolution of the system can be described by solving the master equation [50]

$$\frac{\partial \rho}{\partial t} = -\frac{i}{\hbar}[H,\rho] + L(\rho), \tag{2}$$

where ρ is the density operator and $L(\rho)$ denotes the decoherence processes. And then we obtain the time evolution of density matrix elements as follows:

$$\begin{aligned}
\dot{\rho}_{21} &= -\gamma_{21}\rho_{21} - i\big[\omega_{21}\rho_{21} - \Omega_p e^{-i\omega_p t}(\rho_{22}-\rho_{11}) + \big(-\Omega_{c1}e^{-i\omega_{c1}t} - \Omega_{c2}e^{-i\omega_{c2}t}\big)\rho_{31}\big],\\
\dot{\rho}_{31} &= -\gamma_{31}\rho_{31} - i\big[(\omega_{21}+\omega_{32})\rho_{31} + \Omega_m e^{-i\omega_m t}\rho_{41} + \Omega_p e^{-i\omega_p t}\rho_{32}\\
&\quad + \big(-\Omega_{c1}e^{-i\omega_{c1}t} - \Omega_{c2}e^{-i\omega_{c2}t}\big)\rho_{21}\big],\\
\dot{\rho}_{41} &= -\gamma_{41}\rho_{41} - i\big[(\omega_{21}+\omega_{32}-\omega_{43})\rho_{41} + \Omega_m e^{-i\omega_m t}\rho_{31} + \Omega_p e^{-i\omega_p t}\rho_{42}\big],
\end{aligned} \tag{3}$$

with the closure relationship $\rho_{11} + \rho_{22} + \rho_{33} + \rho_{44} = 1$. $\gamma_{jk} = (\Gamma_j + \Gamma_k)/2$, $\Gamma_j = \sum_k \Gamma_{jk}$ $(j,k = 1,2,3,4)$, where Γ_{jk} is the spontaneous decay rate from state $|j\rangle$ to state $|k\rangle$. We perform a rotating-frame transformation using $\rho_{21} = \tilde{\rho}_{21}e^{-i\omega_p t}$, $\rho_{31} = \tilde{\rho}_{31}e^{-i(\omega_p+\omega_{c1})t}$ and $\rho_{41} = \tilde{\rho}_{41}e^{-i(\omega_p+\omega_{c1}-\omega_m)t}$. The density-matrix element $\tilde{\rho}_{ij}$ can be expanded in terms of Fourier components as

$$\tilde{\rho}_{ij} = \sum \tilde{\rho}_{ij}^{(n)} e^{-in\delta t} \quad \big(i,j \in \{1,2,3,4\}, n = 0, \pm 1, \ldots\big). \tag{4}$$

We keep the first order of the probe and all orders of the control and MW fields, and get

$$\begin{aligned}
\tilde{\rho}_{21}^{(n)} &= \frac{i(\tilde{\rho}_{31}^{(n)}\Omega_{c1} + \tilde{\rho}_{31}^{(n-1)}\Omega_{c2} + \Omega_p)}{\gamma_{21} + i\Delta_p - in\delta}, \\
\tilde{\rho}_{31}^{(n)} &= \frac{-i\tilde{\rho}_{21}^{(n)}\Omega_{c1} - i\tilde{\rho}_{21}^{(n+1)}\Omega_{c2}}{-\gamma_{31} + in\delta - i(\Delta_p + \Delta_{c1}) - \frac{i\Omega_m^2}{i\gamma_{41}+n\delta+\Delta_m-\Delta_p-\Delta_{c1}}}, \\
\tilde{\rho}_{41}^{(n)} &= \frac{\tilde{\rho}_{31}^{(n)}\Omega_m}{i\gamma_{41} + n\delta + \Delta_m - \Delta_p - \Delta_{c1}},
\end{aligned} \tag{5}$$

where $\Delta_p = \omega_p - \omega_{21}$, $\Delta_{c1} = \omega_{c1} - \omega_{32}$ and $\Delta_m = \omega_m - \omega_{43}$ are the detunings of the probe, control and MW fields, respectively. The solution of $\tilde{\rho}_{21}^{(n)}$ is obtained from the recursion relation as

$$\tilde{\rho}_{21}^{(n)} = D_n^{-1}\left[-i\Omega_p + \frac{\tilde{\rho}_{21}^{(n-1)}\Omega_{c1}^*\Omega_{c2}}{X_{n-1}} + \frac{\tilde{\rho}_{21}^{(n+1)}\Omega_{c1}\Omega_{c2}^*}{X_n}\right], \tag{6}$$

where $X_n = -\gamma_{31} + in\delta - i(\Delta_p + \Delta_{c1}) + i\Omega_m^2/(i\gamma_{41} + n\delta + \Delta_m - \Delta_p - \Delta_{c1})$ and $D_n = -\gamma_{21} - i(\Delta_p - n\delta) - \Omega_{c1}^2/X_n - \Omega_{c2}^2/X_{n-1}$. We can obtain the coherent term $\tilde{\rho}_{21}^{(0)}$ with a continued fraction method [42]

$$\tilde{\rho}_{21}^{(0)} = \frac{-i\Omega_p}{D_0 - \frac{\Omega_{c1}\Omega_{c2}^* W_1}{-\gamma_{31}-i(\Delta_p+\Delta_{c1})-\frac{i\Omega_m^2}{i\gamma_{41}+\Delta_m-\Delta_p-\Delta_{c1}}} - \frac{\Omega_{c1}^*\Omega_{c2} V_1}{-\gamma_{31}-i(\Delta_p+\Delta_{c2})-\frac{i\Omega_m^2}{i\gamma_{41}+\Delta_m-\Delta_p-\Delta_{c2}}}}, \tag{7}$$

where $\Delta_{c2} = \Delta_{c1} - \delta$, $W_1 = \tilde{\rho}_{21}^{(1)}/\tilde{\rho}_{21}^{(0)}$ and $V_1 = \tilde{\rho}_{21}^{(1)}/\tilde{\rho}_{21}^{(2)}$. The susceptibility χ is found to be $\chi = N\mu_{21}^2\tilde{\rho}_{21}^{(0)}/\hbar\varepsilon_0\Omega_p$, where ε_0 is the permittivity of vacuum, N is the atomic density, and $\hbar$ is the reduced Planck's constant. The transmission spectrum can be described as [51]

$$T = \exp\left(-2\pi\,\ell\,\mathrm{Im}[\chi]/\lambda_p\right), \tag{8}$$

where ℓ is the medium length and λ_p is the center wavelength of probe field.

3 Results and discussion

We consider the ^{87}Rb atoms within a vapor cell of length 5.0 cm. The probe field, ∼780 nm, is tuned to the $|1\rangle \to |2\rangle$ transition. The control field, ∼480 nm, drives $|2\rangle \to |3\rangle$ transition. The Rydberg transition $|3\rangle \to |4\rangle$ is driven by the MW field. In the following discussion, the parameters are scaled by $\Gamma = 2\pi \times 6$ MHz for simplicity. First, let us briefly discuss the absorption spectra of common EIT scheme. If the MW field $\Omega_m = 0$, there is an EIT window (see red dotted line in Fig. 2(a)). With coupling of the MW field, an absorption peak appears in the EIT window, i.e., bright resonance [11] (see red dotted line in Fig. 2(b)). Here, we are interested in the absorptive features of bichromatic EIT spectra, as shown by the solid blue line in Fig. 2. Without coupling of the MW field, there are four absorption peaks in EIT spectrum (see Fig. 2(a)). When the MW field drives the Rydberg transition, the two side absorption peaks and the central EIT window split, resulting in seven absorption peaks (see Fig. 2(b)).

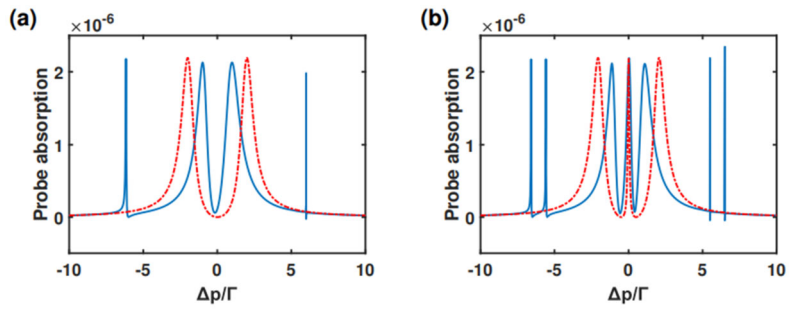

Figure 2 Comparison of absorption spectra driven by bichromatic control field (blue) and single control field (red). (a) $\Omega_m = 0$ and (b) $\Omega_m = 0.5\Gamma$. Other parameters are $\Omega_{c1} = \Omega_{c2} = 1\Gamma$, $\Delta_{c1} = \Delta_m = 0$, $\delta = 6\Gamma$, $\gamma_{21} = \Gamma = 2\pi \times 6$ MHz, $\gamma_{31} = 2\pi \times 1$ kHz and $\gamma_{41} = 2\pi \times 0.5$ kHz

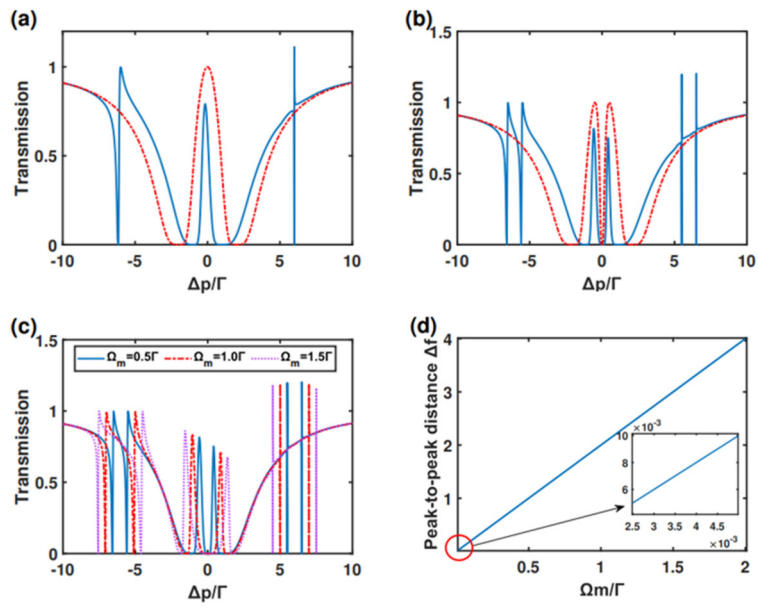

Figure 3 (a) Transmission spectra with $\Omega_m = 0$ and (b) is the same as (a) except for $\Omega_m = 0.5\Gamma$; (c) bichromatic control field-driven transmission spectra with different MW fields; (d) peak-to-peak distance Δf versus MW field strength Ω_m, and other parameters are the same as in Fig. 2

The results can be interpreted in the dressed-state picture, as shown in Fig. 1(b). It is known that the central EIT window originates from inter-path interference of the transitions $|1\rangle \rightarrow |\pm 1\rangle$. The dressed-states created by the bichromatic control field consist of infinite ladders with an equal separation δ [52]. In particular, when Ω_{c1}, $\Omega_{c2} < \delta$, the transition amplitude will be dominant only for a few dressed-states around $|m = 0\rangle$ [35]. The probe transitions from $|1\rangle$ to the dressed-states $|m = \pm 1, \pm 2\rangle$ lead to four absorption peaks. When the Rydberg transition $|3\rangle \rightarrow |4\rangle$ is driven by the MW field Ω_m, five new eigenstates appear, i.e., $|0\rangle$, $|\pm a\rangle$ and $|\pm b\rangle$. So, there are seven transition channels with the coupling of the probe field, $|1\rangle \rightarrow |m = 0, \pm 1, \pm a, \pm b\rangle$, which contribute to seven absorption peaks.

Next, we focus on the bichromatic EIT transmission with the MW fields. If $\Omega_m = 0$, there are three transmission peaks around $\Delta_p = 0, \pm 6\Gamma$ (see blue solid line in Fig. 3(a)). It is con-

sistent with the result of Ref. [35] under the given conditions, e.g., $\Omega_{c1} = \Omega_{c2} = 0.5\Gamma$ and $\Delta_{c1} = \Delta_{c2} = \delta/2 = \Gamma$. When the MW field is applied, e.g., $\Omega_m = 0.5\Gamma$, the three transmission peaks split into six via the EIT-AT effect (see blue solid line in Fig. 3(b)). Figure 3(c) depicts the bichromatic EIT transmission spectra with a varying MW field strength Ω_m. The frequency splitting of transmission peaks becomes larger with the increase of Ω_m. It is interesting to find that the peak-to-peak distance Δf is proportional to the MW field strength, as shown in Fig. 3(d). Their linear relationship can be written as $\Delta f = 2\Omega_m$, and the magnitude of the applied MW E-field can be estimated by

$$|E_m| = \frac{\hbar\Omega_m}{\mu_{34}} = \frac{\hbar\Delta f}{2\mu_{34}}. \tag{9}$$

It is worth mentioning that the frequency splitting of the side peaks also has the good linear relationship with the MW E-field strength. Of course, the linear relationship between Δf and $|E_m|$ will fail and become nonlinear when $\Omega_m < 0.0025\Gamma$.

Moreover, the linewidth of the central transmission peak is much narrower than that of the common EIT transmission peak (see Fig. 3(b)). The linewidth narrowing can be understood from the high dispersion produced by the bichromatic EIT. Figure 4 shows the real ($\mathrm{Re}[\chi]$) and imaginary ($\mathrm{Im}[\chi]$) parts of the atomic susceptibility. The bichromatic EIT dispersion $\partial\,\mathrm{Re}[\chi]/\partial\omega_p$ is larger than that of the common EIT scheme in Fig. 4(a). The larger dispersion, the larger frequency pulling effect, and then the resonance frequency is strongly pulled to its bichromatic EIT frequency. As a result, the two EIT windows are narrowed, resulting in two narrow peaks in the bichromatic EIT transmission (see red dashed line in Fig. 4).

The linewidth can be described as [14]

$$\Delta_{\mathrm{width}} = \frac{\Omega_{c1}^2 + \Omega_p^2}{\sqrt{\Gamma_{21}\gamma_{21}}}\frac{1}{\sqrt{\sigma N\ell}} \quad (\sigma N\ell \gg 1), \tag{10}$$

where $\sigma = 3\lambda_p^2/2\pi$ is the absorption cross section, N is the atomic denstiy, and ℓ is the medium length. The numerical results show that the full width at half maximum (FWHM) of the bichromatic EIT central transmission peaks is about 0.24Γ. While, the FWHM of the common EIT transmission peaks is about 0.9Γ. The linewidth is narrowed to about 1/4 of the common EIT scheme. The spectral resolution is intimately related to the EIT linewidth [21, 53]. This indicates that the spectral resolution could be increased by about

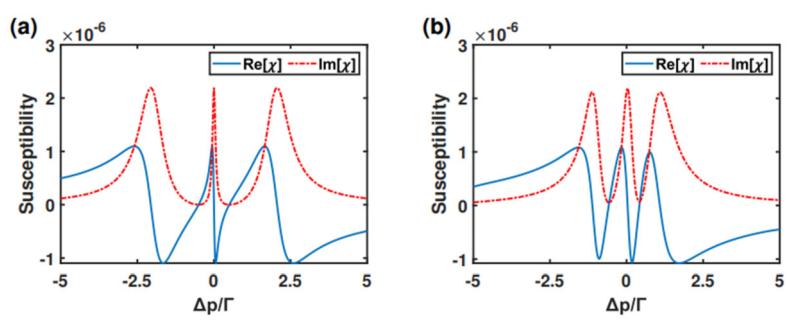

Figure 4 Susceptibility as a function of probe field detuning Δ_p. $\mathrm{Re}[\chi]$ (blue solid line) and $\mathrm{Im}[\chi]$ (red dash line) for (a) single and (b) bichromatic control fields. Other parameters are the same as in Fig. 2

4 times under the given conditions. Moreover, the application of narrow EIT spectrum would compress the nonlinear zoom of frequency splitting and decrease the uncertainty of the MW E-field measurements [54]. So the inter-path interference leads to the narrow EIT spectrum, contributing to the sensitive measurement of MW E-fields.

The minimum detectable strength is important for the weak MW E-field measurement, which depends on the minimum detectable splitting of the transmission peak. In a weak MW field regime, the frequency splitting strongly depends on the EIT linewidth that is related to the Rabi frequency of control (probe) field (see equation (10)) [54]. The frequency splitting Δf decreases as $\Omega_{c1(p)}$ decreases. The minimum detectable strength of the MW E-field is given by [55]

$$|E_{\min}| = \frac{\hbar\Delta_{\text{width}}}{2\mu_{34}}, \tag{11}$$

where $\Delta_{\text{width}} < \Delta f$. The linear relationship between Δf and $|E_m|$ from equation (9) is valid and can be used to determine the E-field strength when the EIT linewidth is small compared to the frequency splitting [15]. This means that the narrow EIT linewidth would enable the frequency splitting to be observed at a weak MW field [21, 26].

According to the Rayleigh criterion [56], the minimum detectable splitting means that the splitting of two peaks is about half maximum of its peak value. For the common EIT scheme, when $\Omega_m = 0.007\Gamma$, the transmission peaks overlap partly and are just discernible, as shown in Fig. 5(a). While, the bichromatic EIT transmission peaks are clearly separated from each other (see Fig. 5(b)). Under the given condition, the minimum detectable strength of the MW field is about $\Omega_m = 0.0025\Gamma$ from the simulation. It is about 1/3 of the common EIT scheme, $\sim 0.007\Gamma$. This indicates that the minimum detectable MW E-field strength could be enhanced about 3 times. In other words, the inter-path interference much narrow the EIT linewidth and improve the sensitivity of minimum MW E-field.

In addition, we consider the longitudinal motion of atoms at randomly distributed velocity v. It is instructive to examine the MW E-field measurement with Doppler effect, i.e., the probe and control fields Ω_{c1} (or Ω_{c1} and Ω_{c2}) co-propagating through the atomic cell. Here, the susceptibility with atomic motion should be expressed as $\chi(v) = N\mu_{21}^2 \int \tilde{\rho}_{21}^{(0)}(v) * D(v)/\hbar\varepsilon_0\Omega_p\, dv$, where Δ_p, Δ_{c1} and Δ_{c2} are replaced with $\Delta_p + k_p v$, $\Delta_{c1} + k_{c1}v$ and $\Delta_{c2} \pm k_{c2}v$ respectively (+ for the x-axis), $D(v) = \exp(-v^2/v_p^2)/\pi^{1/2}v_p$, represents the Maxwell–Boltzmann distribution of atoms, and v_p is the most probable velocity. For simplicity, we assume that the wavevector $|k_p| \approx |k_{c1}| \approx |k_{c2}| \approx |k|$.

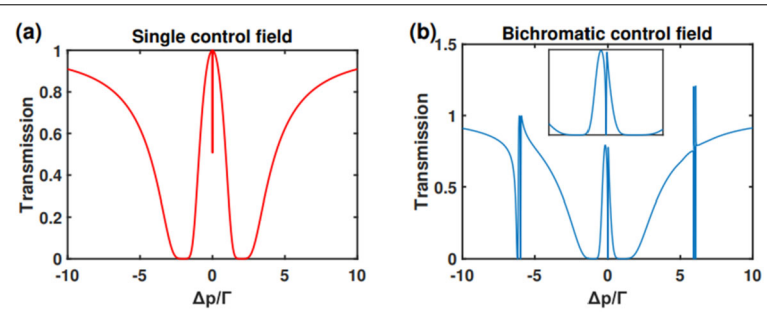

Figure 5 (a) Single control field-driven and (b) bichromatic control field-driven transmission spectra (inset is zoomed views of central peaks), and other parameters are the same as in Fig. 2

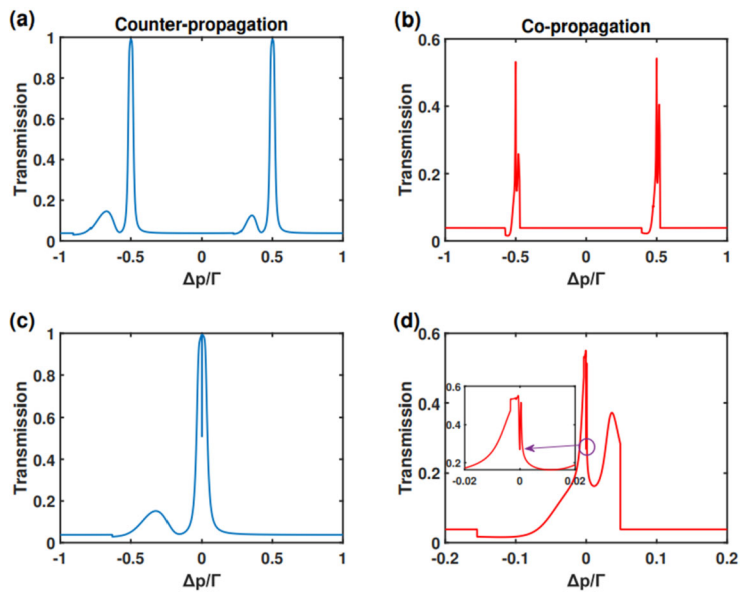

Figure 6 Transmission of the bichromatic control field with Doppler effect for the counter-propagation (a) and co-propagation (b) cases; (c) is the same as (a) except for $\Omega_m = 0.00125\Gamma$ and (d) is the same as (b) except for $\Omega_m = 0.00045\Gamma$ (inset is zoomed views of central peaks). Other parameters are the same as in Fig. 2

Figure 6 shows the Doppler-averaged transmission spectrum. When the control fields Ω_{c1} and Ω_{c2} counter-propagate through the atomic vapor, the central transmission peaks are much narrowed and the side peaks decrease sharply (see Fig. 6(a)). It is consistent with the result of Ref. [36] under the given conditions, e.g., $\Omega_{c1} = \Omega_{c2} = \Gamma$ and $\Delta_{c1} = \Delta_{c2} = \delta/2 = 0.05\Gamma$. This result originates from the shift of the dressed levels and the modification to the transition probability between dressed states when the Doppler effect is considered [57]. The sum of all contributions by atoms with different velocities results in the narrowed transmission spectrum. In this case, the minimum detectable MW field strength is about $\Omega_m = 0.00125\Gamma$, as illustrated in Fig. 6(c). Figure 6(b) depicts the transmission of the control field Ω_{c1} and Ω_{c2} co-propagating with the probe field. The central transmission peaks are further narrowed under the same conditions. The minimum detectable strength of the MW field is about $\Omega_m = 0.00045\Gamma$ from the simulation (see Fig. 6(d)). It is about 1/5 of that without Doppler averaging, $\sim 0.0025\Gamma$. This indicates that the minimal detectable MW E-field strength could be improved by more than 5 times after Doppler averaging.

At last, the effect of frequency detuning on the transmission of the probe field is investigated. Take control fields Ω_{c1} and Ω_{c2} counter-propagation for example, Fig. 7(a) shows the transmission peaks with a varying MW field detuning Δ_m. The peak-to-peak distance Φf is enlarged with an increase in Δ_m, which can be expressed as $\Phi f = (\Delta_m^2 + (2\Omega_m)^2)^{1/2}$. This result is consistent with Ref. [24], and indicates that frequency detuning could improve the sensitivity of MW E-field measurements. In Fig. 7(b), the central transmission peaks shift with the bichromatic control field detuning ($\Delta = \Delta_{c1} = \Delta_{c2}$), while both the linewidth and the peak-to-peak distance basically remain unchanged. The bichromatic EIT scheme shows some tunability and may allow the MW E-field measurement in a broad frequency range.

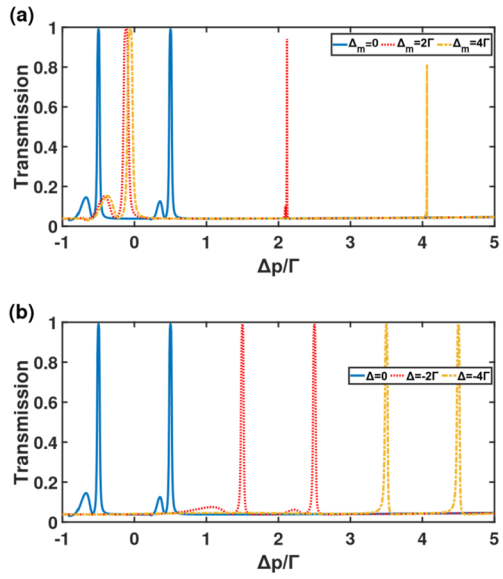

Figure 7 Transmission spectra of the probe field at different MW field detuning (a) and bichromatic control field detuning (b). Other parameters are the same as in Fig. 2

4 Conclusions

In summary, we propose a scheme for MW E-field measurement based on the bichromatic EIT in Rydberg atoms. Due to the inter-channel EIT interference, the EIT spectrum exhibits multiple narrow transmission peaks. It is interesting to find that the frequency splitting of transmission peaks shows a linear relationship with the MW field strength, which can be used to measure the MW E-field. The numerical results show that the spectral resolution may be enhanced by about 4 times, and the minimum detectable strength of the MW E-field is about 3 times larger than that of the common EIT scheme. If the Doppler scheme is adopted, the minimum detectable MW E-field strength could be further increased by about 5 times after Doppler averaging. The bichromatic EIT scheme exhibits high sensitivity, high resolution, and a broad detection range, which may help to design novel MW-sensing devices.

Acknowledgements
The authors appreciate the helpful discussion with Prof. Qingtian Zeng.

Funding
This work was supported by the Shandong Natural Science Foundation, China (No. ZR2021LLZ006), the National Natural Science Foundation of China (NSFC) (Nos. 61675118, 61773245), the National Key Research and Development Program of China (No. 2017YFA0701003), the Taishan Scholars Program of Shandong Province, China (No. ts20190936), the Shandong University of Science and Technology Research Fund, China (No. 2015TDJH102), and the Innovation and entrepreneurship training program for college students of Shandong Province (No. S202110424009).

Availability of data and materials
The datasets used and/or analysed during the current study are available from the corresponding author on reasonable request.

Declarations

Competing interests
The authors declare no competing interests.

Author contributions

M. Han conceived the idea and the schem, derived the theoretical framework and code, performed the calculations and wrote the manuscript. H. Hao conducted the experiment, and analysed data. X. Song contributed to reviewing and editing. Z. Yin , M. Parniak, Z. Jla contributed to reviewing and assessing the results. Y. Peng contributed throughout, supervised the research, and provided funding. All authors reviewed the manuscript.

Author details

[1]Qingdao Key Laboratory of Terahertz Technology, College of Electronic and Information Engineering, Shandong University of Science and Technology, Qingdao 266590, China. [2]Beijing Institute of Radio Measurement, Beijing, China. [3]Centre for Quantum Optical Technologies, Centre of New Technologies, University of Warsaw, Banacha 2c, 02-097 Warsaw, Poland.

Received: 29 March 2023 Accepted: 26 June 2023 Published online: 14 July 2023

References

1. Pan S, Zhang Y. Microwave photonic radars. J Lightwave Technol. 2020;38:5450–84. https://doi.org/10.1109/JLT.2020.2993166.
2. Panda SSS, Panigrahi T, Parne SR, Sabat SL, Cenkeramaddi LR. Recent advances and future directions of microwave photonic radars: a review. IEEE Sens J. 2021;21:21144–58. https://doi.org/10.1109/JSEN.2021.3099533.
3. Wang X, Qin T, Qin Y, Witte RS, Microwave-Induced XH. Thermoacoustic communications. IEEE Trans Microw Theory Tech. 2017;65:3369–78. https://doi.org/10.1109/TMTT.2017.2669970.
4. Meyer DH, Cox KC, Fatemi FK, Digital KPD. Communication with Rydberg atoms & amplitude-modulated microwave fields. Appl Phys Lett. 2018;112:211108. https://doi.org/10.1063/1.5028357.
5. Du Y, Cong N, Wei X, Zhang X, Luo W, He J et al. Realization of multiband communications using different Rydberg final states. AIP Adv. 2022;12:065118. https://doi.org/10.1063/5.0095780.
6. Li X, Wu D, Miao Q, Zhu H, Wei T. A navigation ranging scheme with true random entangled microwave signals. IEEE Photonics J. 2018;10:1–7. https://doi.org/10.1109/JPHOT.2018.2876045.
7. Liu Y, Bao Y. Review of electromagnetic waves-based distance measurement technologies for remote monitoring of civil engineering structures. Measurement. 2021;176:109193. https://doi.org/10.1016/j.measurement.2021.109193.
8. Kim Y, Kimball JS, McDonald KC, Glassy J. Developing a global data record of daily landscape freeze/thaw status using satellite passive microwave remote sensing. IEEE Trans Geosci Remote Sens. 2011;49:949–60. https://doi.org/10.1109/TGRS.2010.2070515.
9. Deb AB, Kjærgaard N. Radio-over-fiber using an optical antenna based on Rydberg states of atoms. Appl Phys Lett. 2018;112:211106. https://doi.org/10.1063/1.5031033.
10. Gallagher TF. Rydberg atoms. Cambridge: Cambridge University Press; 2005.
11. Sedlacek JA, Schwettmann A, Kübler H, Löw R, Pfau T, Shaffer JP. Microwave electrometry with Rydberg atoms in a vapour cell using bright atomic resonances. Nat Photonics. 2012;8:819–24. https://doi.org/10.1038/nphys2423.
12. Tishchenko VA, Tokatly VI, Luk'yanov VI. The beginning of the metrology of radio frequency electromagnetic fields and the first standards of electric field strength. Meas Tech. 2003;46:76–84. https://doi.org/10.1023/A:1023425908932.
13. Holloway CL, Gordon JA, Jefferts S, Schwarzkopf A, Anderson DA, Miller SA et al. Broadband Rydberg atom-based electric-field probe for SI-traceable, self-calibrated measurements. IEEE Trans Antennas Propag. 2018;62:6169–82. https://doi.org/10.1109/TAP.2014.2360208.
14. Fleischhauer M, Imamoglu A, Marangos JP. Electromagnetically induced transparency: optics in coherent media. Rev Mod Phys. 2005;77(2):633–73. https://doi.org/10.1103/RevModPhys.77.633.
15. Holloway CL, Simons MT, Gordon JA, Dienstfrey A, Anderson DA, Raithel G. Electric field metrology for SI traceability: systematic measurement uncertainties in electromagnetically induced transparency in atomic vapor. J Appl Phys. 2017;121:233106. https://doi.org/10.1063/1.4984201.
16. Wang J, Han M, Zhao S, Cai Y, Jelezko F, Jia Z et al. Optical PAM-4 generation via electromagnetically induced transparency in nitrogen-vacancy centers. Results Phys. 2021;30:104802. https://doi.org/10.1016/j.rinp.2021.104802.
17. Zhang S, Zhou S, Loy MMT, Wong GKL, Du S. Optical storage with electromagnetically induced transparency in a dense cold atomic ensemble. Opt Lett. 2011;36(23):4530–2. https://doi.org/10.1364/OL.36.004530.
18. Autler SH, Townes CH. Stark effect in rapidly varying fields. Phys Rev. 1955;100:703–22. https://doi.org/10.1103/PhysRev.100.703.
19. Salloum TYA. Electromagnetically induced transparency and Autle-Townes splitting: two similar but distinct phenomena in two categories of three-level atomic systems. Phys Rev A. 2010;81:053836. https://doi.org/10.1103/PhysRevA.81.053836.
20. You S, Cai M, Zhang S, Xu Z, Liu H. Microwave-field sensing via electromagnetically induced absorption of rb irradiated by three-color infrared lasers. Opt Express. 2022;30(10):16619–29. https://doi.org/10.1364/OE.454433.
21. Liao K, Tu H, Yang S, Chen C, Liu X, Liang J et al. Microwave electrometry via electromagnetically induced absorption in cold Rydberg atoms. Phys Rev A. 2020;101:053432. https://doi.org/10.1103/PhysRevA.101.053432.
22. Yang A, Peng Y, Zhou W, Zhao S, Xu Y, Li Y. Microwave electric-field measurement with active Raman gain. J Opt Soc Am B. 2019;36(8):2134–9. https://doi.org/10.1364/JOSAB.36.002134.
23. Cai Y, Wang J, Lin L, Lu X, Li Y, Peng Y. Proposal of Rydberg atomic receiver for amplitude-modulated microwave signals with active Raman gain. Appl Opt. 2020;59(28):8612–7. https://doi.org/10.1364/AO.399918.
24. Simons MT, Gordon JA, Holloway CL, Anderson DA, Miller SA, Raithel G. Using frequency detuning to improve the sensitivity of electric field measurements via electromagnetically induced transparency and Autler–Townes splitting in Rydberg atoms. Appl Phys Lett. 2016;108:174101. https://doi.org/10.1063/1.4947231.
25. Kumar S, Fan H, Kübler H, Sheng J, Shaffer JP. Atom-based sensing of weak radio frequency electric felds using homodyne readout. Sci Rep. 2017;7:42981. https://doi.org/10.1038/srep42981.
26. Peng Y, Wang J, Yang A, Jia Z, Li D, Chen B. Cavity-enhanced microwave electric field measurement using Rydberg atoms. J Opt Soc Am B. 2018;35:2272–7. https://doi.org/10.1364/JOSAB.35.002272.

27. Peng Y, Zhang Z, Wang X, Liu S, Yang A, Wang X. Frequency and intensity readouts of micro-wave electric field using Rydberg atoms with Doppler effects. Opt Quantum Electron. 2018;50:311. https://doi.org/10.1007/s11082-018-1579-9.
28. Lin L, He Y, Yin Z, Li D, Jia Z, Zhao Y et al. Sensitive detection of radio-frequency field phase with interacting dark states in Rydberg atoms. Appl Opt. 2022;61:1427–33. https://doi.org/10.1364/AO.449918.
29. Yang A, Peng Y, Xu Y, Liang M. Dispersion readout of micro-wave electric field using double-dark-state Rydberg atoms. Laser Phys. 2019;29:045201. https://doi.org/10.1088/1555-6611/ab036b.
30. Peng Y, Zhang Z, Wang J, Chen B, Zeng Q, Li Y. Tunable nonlinear measurement of microwave electric fields with a dressed-state analysis. Eur Phys J D. 2019;73:220. https://doi.org/10.1140/epjd/e2019-100154-0.
31. Liu Z, Zhang L, Liu B, Zhang Z, Guo G, Ding D et al. Deep learning enhanced Rydberg multifrequency microwave recognition. Nat Commun. 2022;13:1997. https://doi.org/10.1038/s41467-022-29686-7.
32. Ficek Z, Freedhoff HS. Resonance-auorescence and absorption spectra of a two-level atom driven by a strong bichromatic field. Phys Rev A. 1993;48:4530–2. https://doi.org/10.1103/PhysRevA.48.3092.
33. Zhu Y, Wu Q, Lezama A, Gauthier DJ, Mossberg TW. Resonance fluorescence of two-level atoms under strong bichromatic excitation. Phys Rev A. 1990;41:6574(R). https://doi.org/10.1103/PhysRevA.41.6574.
34. Freedhoff H, Chen Z. Resonance fluorescence of a two-level atom in a strong bichromatic field. Phys Rev A. 1990;41:4530–2. https://doi.org/10.1103/PhysRevA.41.6013.
35. Wang J, Zhu Y, Jiang KJ, Zhan MS. Bichromatic electromagnetically induced transparency in cold rubidium atoms. Phys Rev A. 2003;68:063810. https://doi.org/10.1103/PhysRevA.68.063810.
36. Yan H, Liao K, Li J, Du Y, Zhang Z, Zhu S. Bichromatic electromagnetically induced transparency in hot rubidium atoms. Phys Rev A. 2013;87:055401. https://doi.org/10.1103/PhysRevA.87.055401.
37. Yang GQ, Xu P, Wang J, Zhu Y, Zhan MS. Four-wave mixing in a three-level bichromatic electromagnetically induced transparency system. Phys Rev A. 2010;82:045804. https://doi.org/10.1103/PhysRevA.82.045804.
38. Emil VD, Andreas K, Florian K, Marten R. Bichromatic four-wave mixing and quadrature-squeezing from biexcitons in atomically thin semiconductor microcavities. Phys Rev B. 2022;106:195307. https://doi.org/10.1103/PhysRevB.106.195307.
39. Li Y, Zhang S, Wei J, Wei J, Ahmed I, Luo B et al. Spatial and frequency dressed multimode of cascaded two spontaneous four-wave mixing. J Opt Soc Am B. 2023;40(4):721–9. https://doi.org/10.1364/JOSAB.482581.
40. Hu M, Qin Z, Che J, Zhang Y. Propagating multi-channel four-wave mixing process in the modulated moving photonic band gap. Opt Express. 2020;28:33448–55. https://doi.org/10.1364/OE.403411.
41. Zhang J, Zhou H, Wang D, Zhu S. Enhanced reflection via phase compensation from anomalous dispersion in atomic vapor. Phys Rev A. 2011;83:053841. https://doi.org/10.1103/PhysRevA.83.053841.
42. Zhou H, Wang D, Wang D, Zhang J, Zhu S. Efficient reflection via four-wave mixing in a Doppler-free electromagnetically-induced-transparency gas system. Phys Rev A. 2011;84:053835. https://doi.org/10.1103/PhysRevA.84.053835.
43. Han M, He Y, Li Q, Song X, Wang Y, Yang A et al. Efficient optical isolator via dual-Raman process with chiral nonlinearity. Results Phys. 2023;46:106288. https://doi.org/10.1016/j.rinp.2023.106288.
44. Li J, Yu R, Ding C, Wu Y. Optical bistability and four-wave mixing with a single nitrogen-vacancy center coupled to a photonic crystal nanocavity in the weak-coupling regime. Opt Express. 2014;22:15024–38. https://doi.org/10.1364/OE.22.015024.
45. Fanid AT, Rostami A. A proposal for optomechanical bichromatic wavelength switching for two-color up-conversion application. Opt Quantum Electron. 2022;54:532. https://doi.org/10.1007/s11082-022-03906-2.
46. Jiang C, Cui Y, Bian X, Li X, Chen G. Control of microwave signals using bichromatic electromechanically induced transparency in multimode circuit electromechanical systems. Chin Phys B. 2016;25(5):054204. https://doi.org/10.1088/1674-1056/25/5/054204.
47. Deng L, Gain-Assisted PMG. Large and rapidly responding Kerr effect using a room-temperature active Raman gain medium. Phys Rev Lett. 2007;98:253902. https://doi.org/10.1103/PhysRevLett.98.253902.
48. Zhang J, Qi T, Pan X, Guo J, Zhu K, Liu X. Helicity of harmonic generation and attosecond polarization with bichromatic circularly polarized laser fields. Chin Phys B. 2019;28(10):103204. https://doi.org/10.1088/1674-1056/ab4176.
49. Scully MO, Zubairy MS. Quantum optics. Cambridge: Cambridge University Press; 1997.
50. Shahriara MS, Wanga Y, Krishnamurthya S, Tua Y, Patic GS, Tsenga S. Evolution of an N-level system via automated vectorization of the Liouville equations and application to optically controlled polarization rotation. J Mod Opt. 2014;61(4):351–67. https://doi.org/10.1080/09500340.2013.865806.
51. Yariv A. Quantum electronics. 3rd ed. Central Book Co.; 1985.
52. Zhu Y, Wu Q, Lezama A, Gauthier DJ, Mossberg TW. Resonance fluorescence of two-level atoms under strong bichromatic excitation. Phys Rev A. 1990;41:5374(R). https://doi.org/10.1103/PhysRevA.41.6574.
53. Zhou F, Jia F, Liu X, Yu Y, Mei J, Zhang J et al. Improving the spectral resolution and measurement range of quantum microwave electrometry by cold Rydberg atoms. J Phys, B At Mol Opt Phys. 2023;56:025501. https://doi.org/10.1088/1361-6455/acae4f.
54. Hao L, Xue Y, Fan J, Jiao Y, Zhao J, Jia S. Rydberg electromagnetically induced transparency and Autler–Townes splitting in a weak radio-frequency electric field. Chin Phys B. 2019;28(5):053202. https://doi.org/10.1088/1674-1056/28/5/053202.
55. Gordon JA, Simons MT, Haddab AH, Holloway CL. Weak electric-field detection with sub-1 Hz resolution at radio frequencies using a Rydberg atom-based mixer. AIP Adv. 2019;9(4):045030. https://doi.org/10.1063/1.5095633.
56. Smith DG. Rayleigh criterion. Field guide to physical optics. 2013.
57. Zhang L, Jiang Y, Wan R, Tian S, Zhang B, Zhang X et al. Extremely narrowed and amplified gain spectrum induced by the Doppler effect. J Phys, B At Mol Opt Phys. 2011;44:135505. https://doi.org/10.1088/0953-4075/44/13/135505.

Publisher's Note